Nanoscale Advances

ROYAL SOCIETY OF CHEMISTRY

PAPER

Cite this: *Nanoscale Adv.*, 2023, **5**, 3104

First-principles examination of two-dimensional Janus quintuple-layer atomic structures $XCrSiN_2$ (X = S, Se, and Te)

P. T. Linh Tran, [a] Nguyen V. Hieu,[b] Hoi Bui D., [c] Q. Nguyen Cuong [de] and Nguyen N. Hieu *[de]

In this work, we propose novel two-dimensional Janus $XCrSiN_2$ (X = S, Se, and Te) single-layers and comprehensively investigate their crystal structure, electronic properties, and carrier mobility by using a first-principles method. These configurations are the combination of the $CrSi_2N_4$ material and a transition metal dichalcogenide. The X-Cr-SiN_2 single-layers are constructed by replacing the N–Si–N atomic layer on one side with chalcogen atoms (S, Se, or Te). The structural characteristics, mechanical or thermal stabilities, and electronic properties are investigated adequately. All three examined configurations are energetically stable and are all small-bandgap semiconductors (<1 eV). Since the mirror symmetry is broken in the Janus material, there exists a remarkable built-in electric field and intrinsic dipole moment. Therefore, the spin–orbit interaction is considered intensively. However, it is observed that the spin–orbit coupling has insignificant effects on the electronic properties of $XCrSiN_2$ (X = S, Se, and Te). Moreover, an external electric field and strain are applied to evaluate the adjustment of the electronic features of the three structures. The transport properties of the proposed configurations are calculated and analyzed systematically, indicating the highly directional isotropy. Our results suggest that the proposed Janus $XCrSiN_2$ could be potential candidates for various applications, especially in nanoscale electronic devices.

Received 21st April 2023
Accepted 5th May 2023

DOI: 10.1039/d3na00261f

rsc.li/nanoscale-advances

1 Introduction

Two-dimensional (2D) materials have attracted interest in not only theoretical but also experimental studies due to their unique physicochemical characteristics. The distinct properties compared to the corresponding bulk phases make 2D materials become potential candidates for tremendous applications such as energy conversion, spintronics,[1–4] piezoelectric materials,[5] photocatalysts,[6] or supercapacitors,[7] *etc.* Currently, there are considerable types of 2D materials studied widely, including graphene,[8,9] transition metal dichalcogenides,[10–12] post-transition metal monochalcogenides,[13–15] stanene,[16] or germanene.[17]

Currently, Janus single-layers are notably interested as a promising candidate for new 2D nanostructures.[18–21] Janus materials possess asymmetric structures due to the lacking of vertical symmetry, leading to many new electronic and photocatalytic properties. Most of the synthesized or proposed Janus structures recently are based on binary or ternary TMDs. Since septuple-atomic-layer $MoSi_2N_4$ was successfully synthesized[22] *via* chemical vapor deposition, these materials have been studied extensively. The $MoSi_2N_4$ single-layer exhibited indirect semiconducting behavior and excellent ambient stability. Recently, Gao and co-workers proposed different nanodevices based on the $MoSi_2P_4$ monolayer, including p–i–n junction field-effect transistors, p–n junction diodes, and photoelectric transistors.[23] In our previous work,[24] we proposed and theoretically investigated the five-atomic-layer Janus $SMoSiN_2$ single-layers that could be obtained from $MoSi_2N_4$ through the substitutions of S atoms for N–Si–N atoms on one side. The Janus $SMoSiN_2$ single-layer exhibits a direct-bandgap semiconducting characteristic. Interestingly, our obtained result indicates that the introduction of S atoms to replace the N–Si–N atoms on one side of the $MoSi_2N_4$ single-layer results in an enhancement of the energy bandgap value and causes the indirect–direct bandgap transition in the considered semiconductor. Then, brand-new heterostructures of the $MoSi_2N_2$ single-layer were proposed as potential configurations in various applications. Following that research subjects, in the current work, our group proposes the asymmetric atomic structures $XCrSiN_2$ (X = S, Se, Te) that are constructed from $CrSi_2N_4$ by substituting N–Si–N atoms by chalcogen atoms (S,

[a]*Faculty of Physics, Hanoi National University of Education, Hanoi 100000, Viet Nam*
[b]*Physics Department, The University of Danang – University of Science and Education, Da Nang, 550000, Viet Nam*
[c]*Faculty of Physics, University of Education, Hue University, Hue 530000, Viet Nam*
[d]*Institute of Research and Development, Duy Tan University, Da Nang 550000, Viet Nam. E-mail: hieunn@duytan.edu.vn*
[e]*Faculty of Natural Sciences, Duy Tan University, Da Nang 550000, Viet Nam*

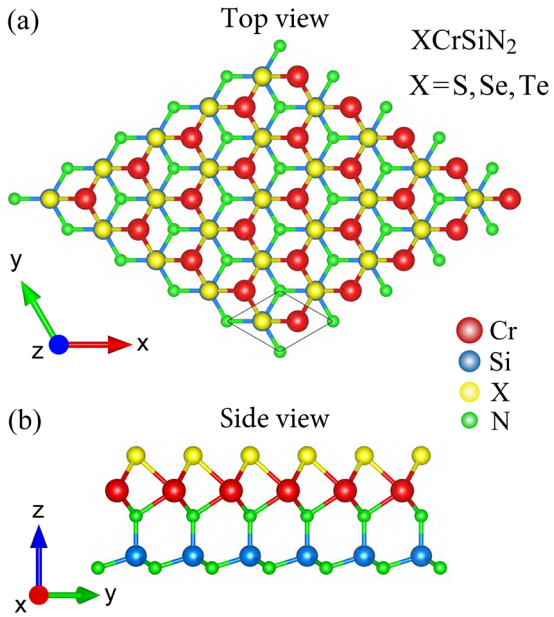

Fig. 1 Top (a) and side (b) views of the crystal structure of $XCrSiN_2$ (X = S, Se, Te) single-layers.

Se, and Te). They can be regarded as a 2D Janus material with mirror symmetry breaking resulting in several extraordinary properties.

In this work, we first optimize the crystal structures of three proposed Janus single-layers $XCrSiN_2$ (X = S, Se, Te) and verify their mechanical and thermal stabilities by performing the first-principles calculations of phonon dispersion and *ab initio* molecular dynamics (AIMD) calculations. Importantly, the electronic properties are investigated and strictly analyzed through the band structures and weighted band structures of all three configurations. Additionally, we investigate how the electronic states of $XCrSiN_2$ single-layers are affected by extrinsic factors, such as mechanical strain and external field. Since the mirror symmetry is broken, resulting in a significant difference in electronegativity of the N–Si–N atomic layer and chalcogen atoms, it is expected that the carrier mobilities, hence the generation/combination of electron–hole pairs, are influenced. Therefore, besides structural and electronic properties, in this work, we also discover electronic transport characteristics.

2 Computational method

The simulations in the present work were carried out by using the density functional method (DFT) as implemented by the Quantum Espresso code.[25] We used the generalized gradient approximation (GGA) of Perdew–Burke–Ernzerhof (PBE)[26] to consider the exchange-correlation functionals. The first Brillouin zone was sampled by $(15 \times 15 \times 1)$ k-point grid using the Monkhorst–Pack model.[27] The cutoff energy for plane waves was set at 50 Ry. The convergence threshold for energy and forces was adopted to be 10^{-6} eV and 10^{-3} eV Å^{-1}, respectively. Besides, we also used the semiempirical DFT-D3 approach[28] to treat the weak van der Waals forces in the examined layered materials. The vertical vacuum distance of 20 Å was inserted to reduce interactions that may exist between periodic images. The AIMD simulations with the NVT ensemble[29] were performed within 8 ps (time step of 1 fs) to test the thermodynamic stability. We used a $6 \times 6 \times 1$ supercell for the AIMD simulations. The deformation potential theory by Bardeen and Shockley was used to evaluate the carrier mobility in the studied single-layers.[30]

3 Calculated results and discussion

3.1 Crystal lattice

The crystal structures of $XCrSiN_2$ (X = S, Se, Te) single-layers belong to the space group $P3m1$ (point group C_{3v}). The optimized crystal structures of the $XCrSiN_2$ (X = S, Se, Te) configurations are presented in Fig. 1, where the stacking order of atomic layers is X–Cr–N–Si–N. The largest lattice constant is found for $TeCrSiN_2$ of 2.99 Å, followed by those of $TeCrSiN_2$ (2.91 Å) and $SCrSiN_2$ (2.87 Å). The cation–cation bond lengths and the thicknesses of the single-layers are also evaluated and listed in Table 1. Similarly, those values are found to decrease in the order of $TeCrSiN_2$, $SeCrSiN_2$, and $SCrSiN_2$ single-layers. The discrepancies in the obtained lattice constants, bond lengths, and thicknesses are attributed to the dissimilarity of the ionic radii of Se, Te, and S ions. The obtained lattice constant of $XCrSiN_2$ is higher than that of $CrSi_2N_4$ (2.84 Å).[31]

By calculating and then analyzing the cohesive energy E_{coh}, the chemical bond strength is examined to confirm the structural stability of these suggested Janus structures. The cohesive energy can be calculated from the following expression

$$E_c = \frac{E_{tot} - (N_{Cr}E_{Cr} + N_{Si}E_{Si} + N_N E_N + N_X E_X)}{N_{Cr} + N_{Si} + N_N + N_X}, \quad (1)$$

where E_{Cr}, E_{Si}, E_N, E_X are the single-atom energies of Cr, Si, N, and X, respectively; E_{tot} is the total energy of the $XCrSiN_2$ single-layer; and N_{Cr}, N_{Si}, N_N, and N_X are the atom number of Cr, Si, N, and X in the unit cell, respectively. The negative value indicates that the structure is stable. Hence, all of the three proposed Janus $XCrSiN_2$ (X = S, Se, Te) single-layers are energetically stable with the cohesive energies of −7.93, −7.71, and −7.38 eV

Table 1 Lattice constant a (Å), chemical bond length d (Å), thickness h (Å), cohesive energy E_c (eV per atom), elastic constants C_{ij} (N m^{-1}), Young's modulus Y_{2D} (N m^{-1}), and Poisson's ratio ν. N(b) and N(m) refer to the N atom located at the bottom and in the middle of the single layer

	a	d_{Cr-X}	d_{Cr-N}	$d_{Si-N(b)}$	$d_{Si-N(m)}$	h	E_c	C_{11}	C_{12}	C_{66}	Y_{2D}	ν
$SCrSiN_2$	2.87	2.26	1.99	1.74	1.74	4.90	−7.93	326.66	90.62	118.02	301.52	0.277
$SeCrSiN_2$	2.91	2.39	2.00	1.76	1.74	5.02	−7.71	316.75	85.19	115.78	293.84	0.269
$TeCrSiN_2$	2.99	2.59	2.01	1.79	1.75	5.18	−7.38	307.02	84.56	111.23	283.73	0.275

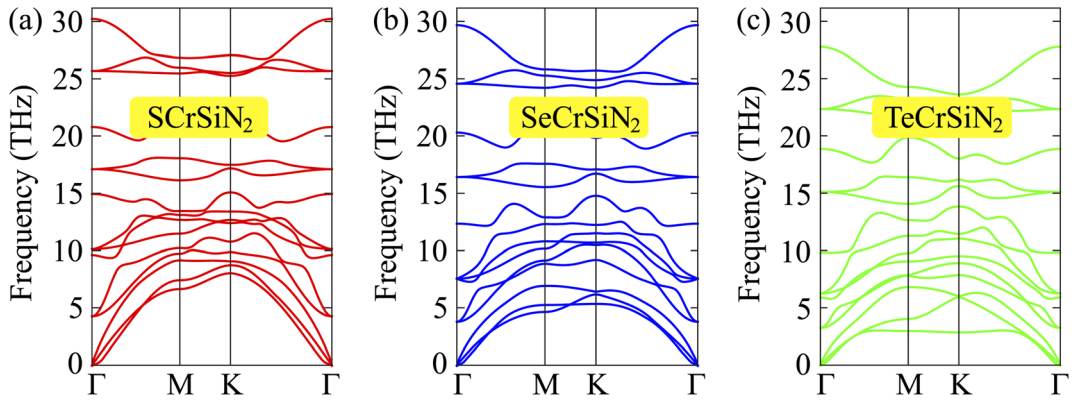

Fig. 2 Phonon dispersions of (a) $SCrSiN_2$, (b) $SeCrSiN_2$, and (c) $TeCrSiN_2$ single-layers.

per atom for $SCrSiN_2$, $SeCrSiN_2$, and $TeCrSiN_2$, respectively. The most stable structure is found for $SCrSiN_2$ that can be expected from the above calculated optimized structure.

Moreover, accurate phonon calculations along the high symmetry line Γ–M–K–Γ are performed to investigate the dynamic stability of the three $XCrSiN_2$ configurations. It is observed from Fig. 2 that there are fifteen vibrational branches (three acoustic and twelve optical modes) since there are five atoms in the primitive cell. In case the negative frequencies are available, there are no restoring forces against the atom displacement. The absence of the soft phonon modes of $XCrSiN_2$ indicates the dynamic stability of these structures. No gap can be observed between the acoustic and optical branches demonstrating a quite high scattering process rate, *i.e.* the lattice thermal conductivity is relatively low. Besides, we also investigated the thermal stability of $XCrSiN_2$ (X = S, Se, Te) structures by means of AIMD simulations at 300 K as presented in Fig. 3. It can be seen that the total potential energies in all three structures fluctuated insignificantly, about 0.3 eV, and were almost unchanged during the whole simulation. Hence, the vibration of constituent atoms is slight and only around the equilibrium positions, so that the chemical bonds remain robust.

Next, the mechanical stability of Janus structures is investigated by calculating and analyzing the elastic constants in accordance with mechanical stability conditions suggested by Born and Huang.[32] In general, for 2D materials, it is necessary to test four independent elastic constants, namely C_{11}, C_{22}, C_{12}, and C_{66} (in Voigt notation). As shown in Fig. 1a, the considered material has a hexagonal structure resulting in $C_{11} = C_{22}$. Consequently, the three following elastic constants are calculated, C_{11}, C_{12} and C_{66}, in which C_{66} is related to C_{11} and C_{12} by the equation $C_{66} = (C_{11} - C_{12})/2$. The obtained results C_{ij} are tabulated in Table 1. It is found that all the elastic constants C_{ij} decrease as the chalcogen element's atomic size increases. In more detail, C_{11} is ranging from 326.66 to 307.02 N m^{-1}, C_{12} is ranging from 90.62 to 84.56 N m^{-1} and C_{66} is ranging from 118.02 to 111.23 N m^{-1} in the order of S, Se, and Te chalcogens. The elastic constants of current Janus structures $XCrSiN_2$ meet Born–Huang's criteria for the hexagonal lattice as $C_{11} > 0$, $C_{11} > C_{12}$, and $C_{66} > 0$,[33] indicating their structures to be mechanically stable.

The mechanical features are also characterized by Young's modulus and Poisson's ratio, which can be calculated from C_{ij}.

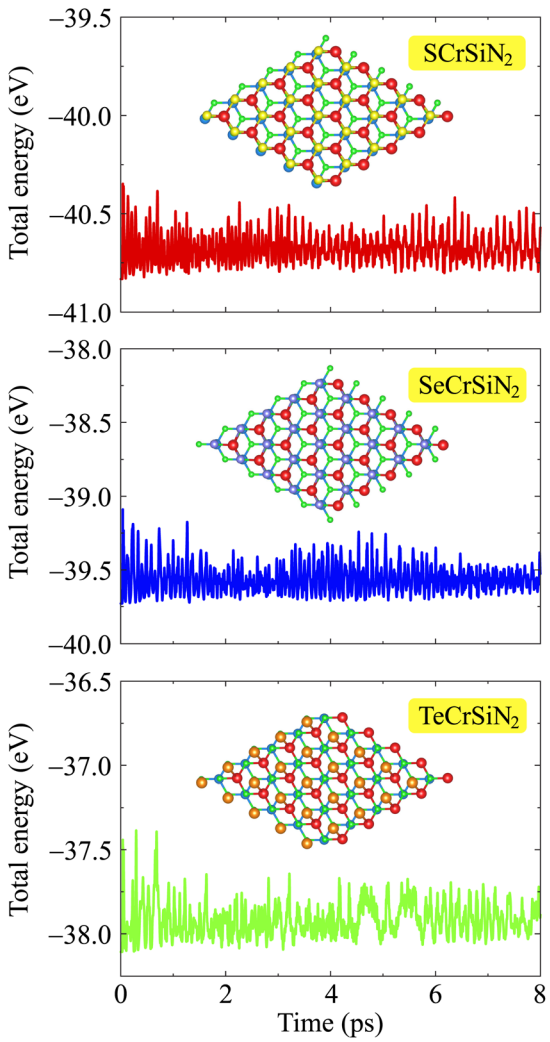

Fig. 3 AIMD calculations for the variations of the total energies to time of $XCrSiN_2$ single-layers at 300 K. Insets are the crystal structures of the corresponding single layers at the end of the AIMD test.

The direction-dependent 2D Young's modulus (in-plane stiffness) $Y_{2D}(\theta)$ and Poisson's ratio $\nu(\theta)$ can be defined as[34,35]

$$Y_{2D}(\theta) = \frac{C_{11}C_{22} - C_{12}^2}{C_{11}\sin^4\theta + C_{22}\cos^4\theta - (2C_{12} - A)\sin^2\varphi\cos^2\theta}, \quad (2)$$

$$\nu(\theta) = \frac{C_{12}(\sin^4\theta + \cos^4\theta) - (C_{11} + C_{22} - A)\sin^2\theta\cos^2\theta}{C_{11}\sin^4\theta + C_{22}\cos^4\theta - (2C_{12} - A)\sin^2\theta\cos^2\theta}, \quad (3)$$

where $A = (C_{11}C_{22} - C_{12}^2)/C_{66}$ and θ is the angle relative to the armchair direction. In Fig. 4, we show the polar diagrams of $Y_{2D}(\theta)$ and $\nu(\theta)$ of $XCrSiN_2$. The angle-dependent $Y_{2D}(\theta)$ and $\nu(\theta)$ profiles in all three structures display perfect circles. Hence, the Janus $XCrSiN_2$ single-layers possess isotropic elastic properties. The values of Young's modulus and Poisson's ratio are listed in Table 1. Young's modulus has a similar trend to the elastic constants C_{ij}, *i.e.*, it decreases with increasing atomic radius X. This means that, under the in-plane external force, $SCrSiN_2$ is the easiest one to be deformed, followed by $SeCrSiN_2$ and $TeCrSiN_2$ single-layers. In comparison to the Cr–Se and Cr–S bonds, the Cr–Te bonds are the longest and most deformable, and these findings are in good agreement with the study discussed above. On the other hand, Poisson's ratio $\nu(\theta)$ appears differently: the highest value of $\nu(\theta)$ is found for the $SCrSiN_2$ single-layer, followed by that of the $TeCrSiN_2$ single-layer, then that of the $SeCrSiN_2$ single-layer. However, the discrepancy in Poisson's ratio is insignificant. Moreover, the Poisson's ratio values are calculated to be positive indicating the trend of contraction (expansion) in the perpendicular direction when there is a tensile (compressive strain) in a certain direction. The Poisson's ratio values are small (ranging from 0.269 to 0.277), indicating all of these single layers are brittle ($\nu < 0.31$).[36]

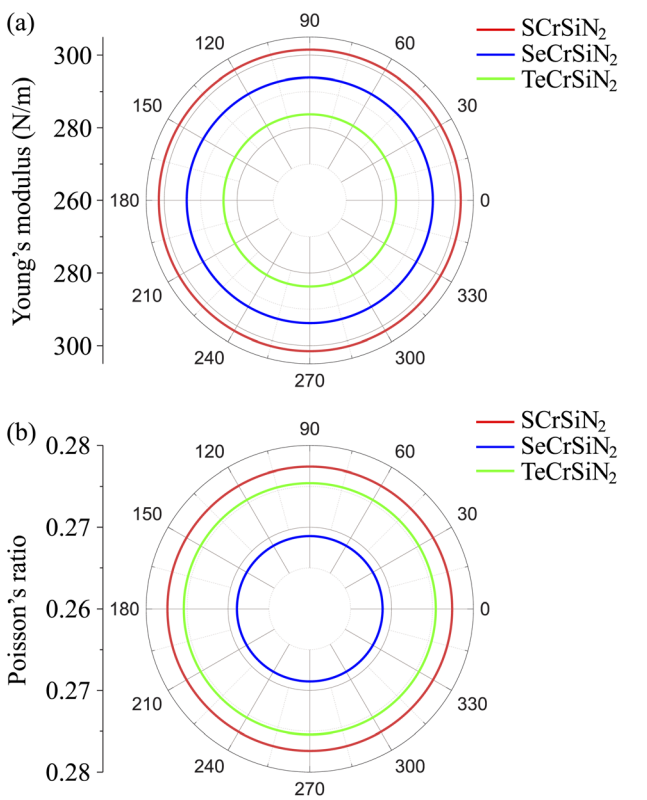

Fig. 4 Polar diagrams for (a) Young's modulus and (b) Poisson's ratio of $XCrSiN_2$.

3.2 Electronic properties

Along with verifying the structural and dynamic stability, the electronic properties are taken into account by evaluating the band structures. In this work, both PBE and PBE + SOC functionals are utilized in order to examine precisely the energy gaps and other electronic properties of the $XCrSiN_2$ (X = S, Se, Te) single-layers. The obtained band structures are presented in

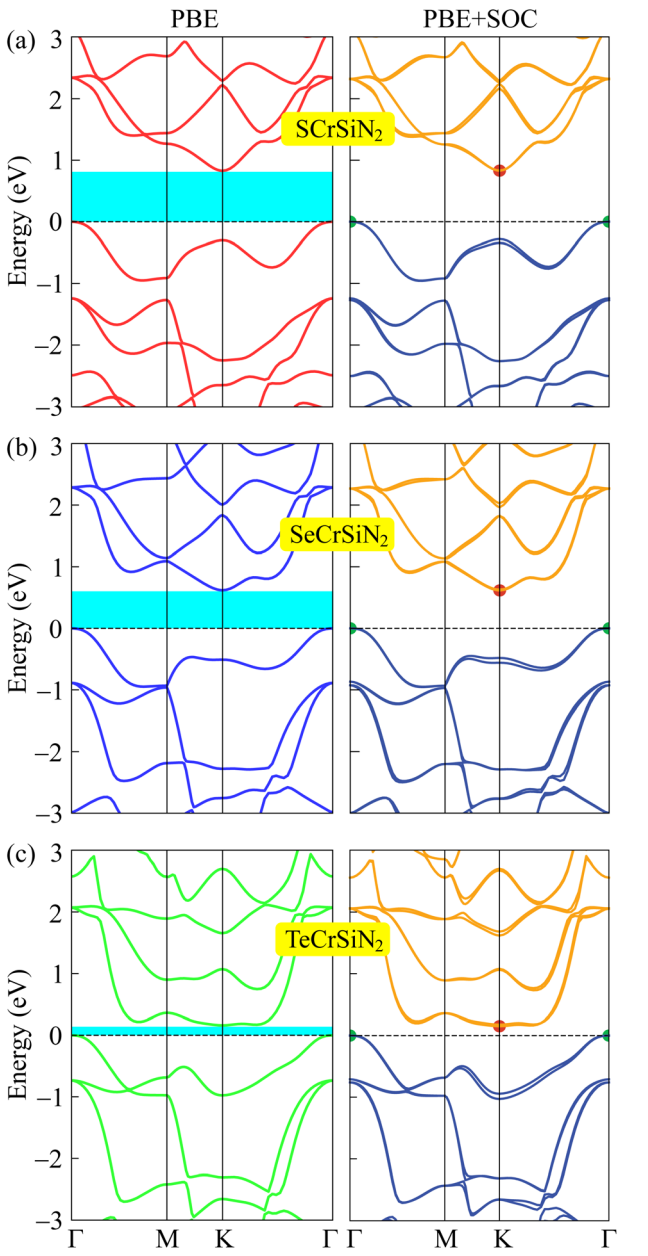

Fig. 5 Calculated band structures of (a) $SCrSiN_2$, (b) $SeCrSiN_2$, and (c) $TeCrSiN_2$ single-layers by using the PBE and PBE + SOC methods. The Fermi level is set at 0 eV.

Table 2 The PBE and PBE + SOC bandgaps E_g, vacuum level difference $\Delta\Phi$, work functions Φ on X and N surfaces of $XCrSiN_2$ single-layers. All parameters are in the units of eV

	E_g^{PBE}	$E_g^{PBE+SOC}$	$\Delta\Phi$	Φ_N	Φ_X
$SCrSiN_2$	0.83	0.83	0.26	5.52	5.26
$SeCrSiN_2$	0.62	0.61	1.07	5.38	4.31
$TeCrSiN_2$	0.16	0.15	1.91	5.09	3.18

Fig. 5 and the energy bandgaps are reported in Table 2. It is calculated that the PBE bandgaps of $SCrSiN_2$, $SeCrSiN_2$, and $TeCrSiN_2$ monolayers are 0.83, 0.62, and 0.16 eV, respectively. The indirect bandgap of $XCrSiN_2$ is comparable with that of $CrSi_2N_4$ (0.49 eV). It is obvious that the band structures have the same profiles and the bandgaps calculated using PBE and PBE + SOC functionals are similar. This suggests that for these current structures, the SOC effect could be neglected to reduce computational cost without any significant difference.

From Fig. 5, we can observe that $XCrSiN_2$ single-layers exhibit small-bandgap semiconductor characteristics with the bandgaps decreasing as the atomic size of chalcogen X increases (S, Se, and Te). All three configurations are indirect semiconductors because the CBM and VBM are located at K and Γ points, respectively. Besides, the PBE-weighted bands of $XCrSiN_2$ are illustrated in Fig. 6 in order to investigate the contribution of each orbital to the electronic energy bands. It can be observed that the weighted band structures of the three configurations are quite similar. The main contribution to the CBM in $XCrSiN_2$ single-layers is the hybridization of the d-orbital of Cr with the p-orbital of S in $SCrSiN_2$, and with the d-orbital of Se and Te in $SeCrSiN_2$ and $TeCrSiN_2$, respectively. However, the VBM of $XCrSiN_2$ is contributed by the hybridization of the d-orbital of Cr with the p-orbital of N mainly, and

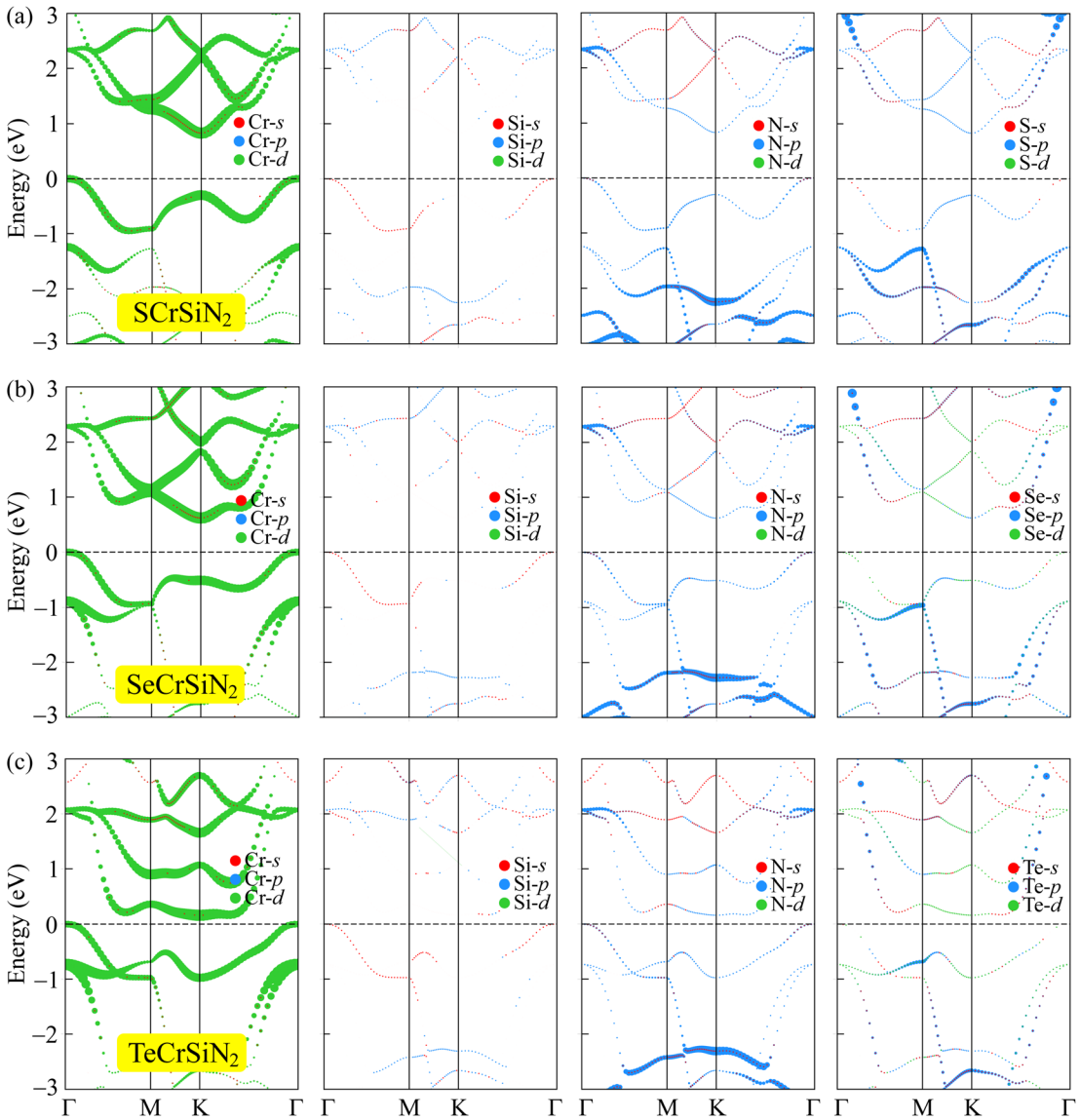

Fig. 6 The PBE weighted bands of (a) $SCrSiN_2$, (b) $SeCrSiN_2$, and (c) $TeCrSiN_2$ single-layers.

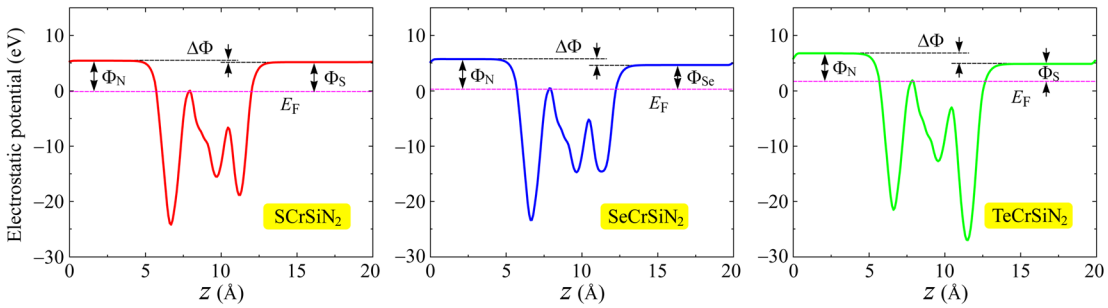

Fig. 7 Electrostatic potentials with the dipole corrections of $XCrSiN_2$ single-layers. The horizontal dashed line indicates the Fermi level.

partly with the p-orbital/d-orbital of the X atom. The Janus $XCrSiN_2$ structures may inhibit the undesirable recombination of photoexcited electron–hole pairs due to their small energy bandgap and different atomic contributions in the CBM and VBM.

Furthermore, we calculate the work function Φ, another important feature of electrons. By calculating the electrostatic potential of the vacuum (Φ_{vac}) and of the Fermi level (Φ_F), the work function Φ can be defined as $\Phi = \Phi_{vac} - \Phi_F$. From Table 2, the Φ_N and Φ_X of the three structures are not much different, implying that electrons have a comparable ability to escape from surfaces of the $XCrSiN_2$ single-layers. Because Janus structures lack vertical mirror symmetry, inherent electric dipoles are introduced, which leads to a discrepancy in the vacuum level on the two surfaces along the z-direction, which can be characterized by $\Delta\Phi$ Fig. 5 presents the planar electrostatic potentials of the $XCrSiN_2$ single-layers where the dipole correction is included.[37] The highest vacuum level difference between two different surfaces ($\Delta\Phi$) is found for $SCrSiN_2$ (0.26 eV), followed by that of $TeCrSiN_2$ (1.91 eV). The smallest work

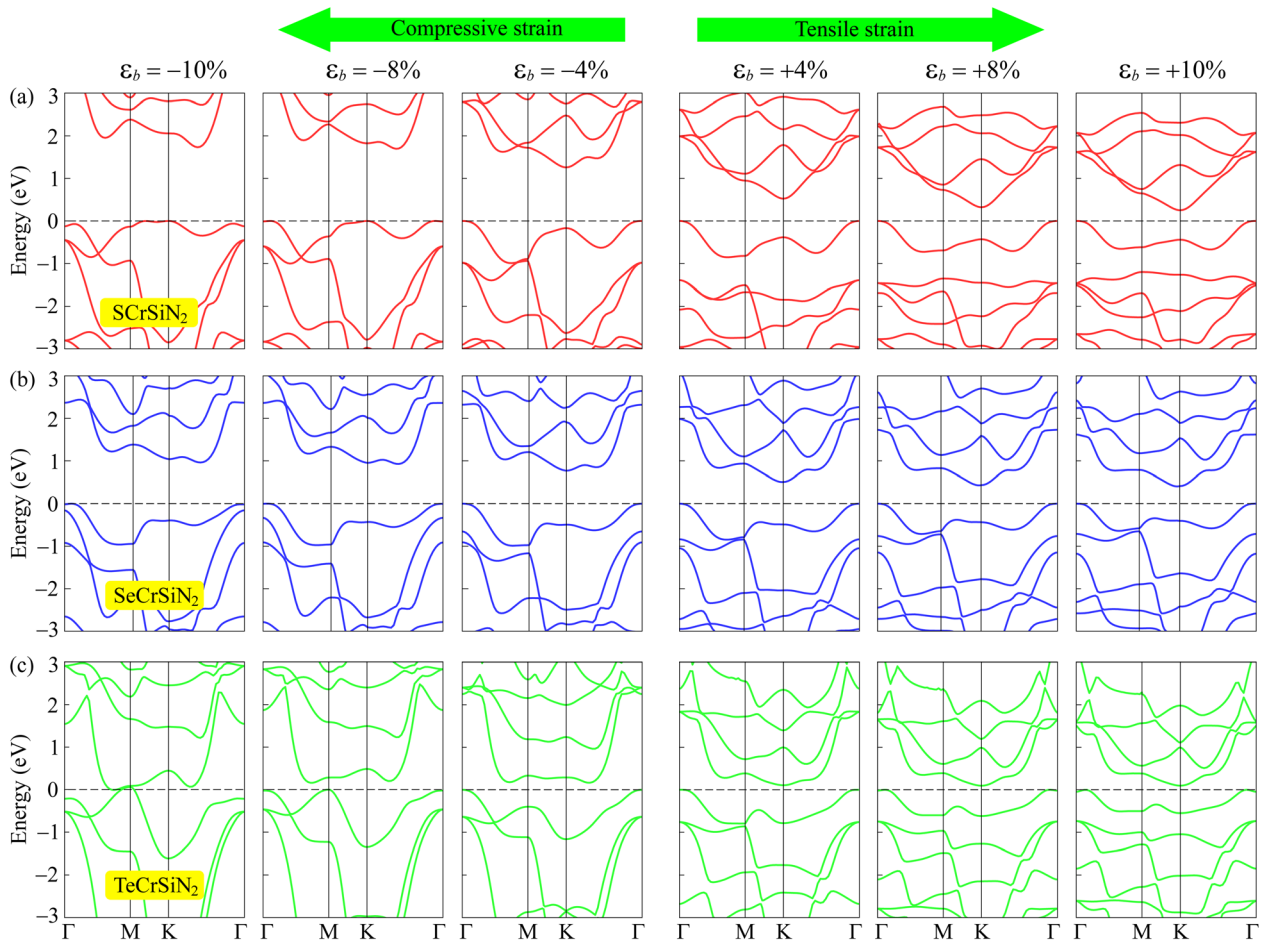

Fig. 8 Band structures of (a) $SCrSiN_2$, (b) $SeCrSiN_2$, and (c) $TeCrSiN_2$ under the biaxial strains ε_b.

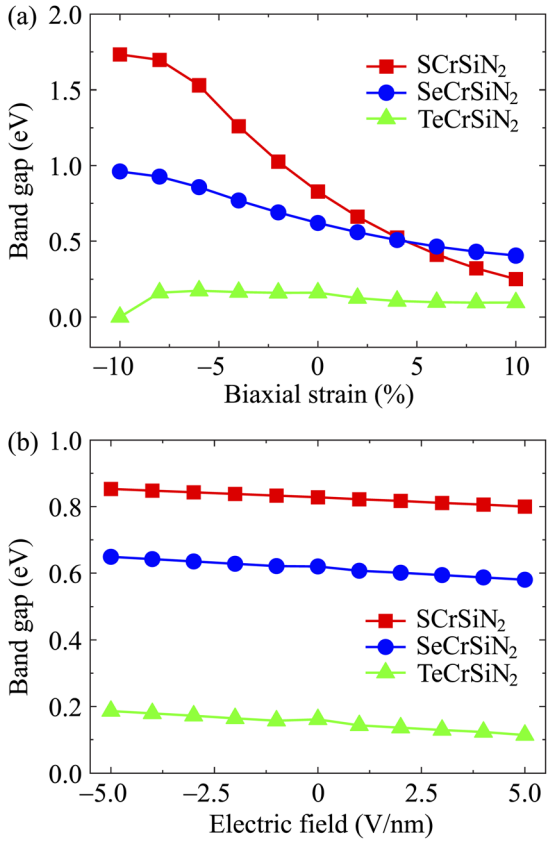

Fig. 9 Bandgaps of $XCrSiN_2$ as functions of the biaxial strain (a) and external electric field (b).

function is found for $SeCrSiN_2$ (1.07 eV), demonstrating that the electrons can escape more easily from the surface of $SeCrSiN_2$ than other structures. These obtained work functions are explained by the slight electronegativity difference between the N and X constituents on the two surfaces (Fig. 7).

It is important to examine the diverse structures under various settings because, as has been reported, the physical properties, particularly the electrical characteristics, of 2D materials are easily modulated by external conditions. Among several approaches, such as doping, heterostructures, *etc.*, strain engineering is one of the simplest but most powerful ways to modulate the electronic structures of 2D nanomaterials. The biaxial strain is defined as $\varepsilon_b = (a - a_0)/a_0$, where a and a_0 are the length of the distorted and undistorted computed cells, respectively. In the current study, we apply a strain of from 0 to ±10%, in which compressive strain is represented by the negative sign and tensile strain by the positive sign. Previous studies[38–42] indicated that the strain could result in a phase transition in 2D structures. In order to evaluate the modification of the electronic states of $XCrSiN_2$, we applied the volumetric expansion to the unit cell of the current three structures and the tuning of electronic properties by strain ε_b is considered. From Fig. 8, it can be observed that the band structures of all three single-layers are altered as the biaxial strains were changed, where the notable change is found to be near the Fermi levels. Fig. 9a depicts the dependence of energy bandgap on the biaxial strain. When the compressive strain increases, the energy bandgaps of both $SCrSiN_2$ and $SeCrSiN_2$ increase, up to about 1.7 and 1.0 eV, respectively. However, for $TeCrSiN_2$, the energy bandgap is almost unchanged when the compressive strain is lower than 10%; and as $\varepsilon_b = -10\%$, the energy bandgap is nearly zero, *i.e.*, there is a transition from a small-bandgap to zero-bandgap semiconductor in $TeCrSiN_2$. When there is tensile strain, the energy bandgap of $SCrSiN_2$ is rapidly decreased (about 0.2 eV as $\varepsilon_b = 10\%$); that of $SeCrSiN_2$ is reduced as well (about 0.5 eV as $\varepsilon_b = 10\%$), and that of $TeCrSiN_2$ is insignificantly changed.

For further investigating the alternative electronic structures under different conditions, besides volumetric strain, an external electric field is next employed to control the electronic structure of examined single-layers. In our modeling, an external electric field is set perpendicular to the 2D plane of materials. The electric field intensity is from -5 V nm^{-1} to +5 V nm^{-1}. The positive (negative) electric fields indicate that the direction is along (opposite to) the positive z-axis. The obtained calculations for energy bandgaps are plotted in Fig. 9b. It can be seen that bandgaps of all three single layers are hardly changed when the electric field is introduced. These results are derived from the band structure calculations (not shown here) in which there is a weak dependence of the band structure on the electric field.

3.3 Carrier mobility

The carrier mobilities and transport characteristics of $XCrSiN_2$ are explored in the final section to examine the migration and separation mechanisms. The suitability of a material for use in electrical devices is mostly determined by the mobility of carriers, especially electrons. It is well-known that there are many efficient ways to calculate carrier mobility, such as

Table 3 Effective mass of carrier m^* (m_0), 2D elastic modulus C_{2D} (N m^{-1}), DP constant E_d (eV), and carrier mobility μ (cm^2 V^{-1} s^{-1}) along the examined directions x and y of $XCrSiN_2$. m_0 is the free electron mass

		m_x^* (m_0)	m_y^* (m_0)	C_{2D}^x (N m^{-1})	C_{2D}^y (N m^{-1})	E_d^x (eV)	E_d^y (eV)	μ_x (cm^2 V^{-1} s^{-1})	μ_y (cm^2 V^{-1} s^{-1})
Electron	$SCrSiN_2$	1.08	1.16	420.84	420.99	−10.49	−10.49	67.01	62.80
	$SeCrSiN_2$	1.53	1.59	403.19	403.54	−10.04	−10.04	35.62	34.44
	$TeCrSiN_2$	5.36	4.78	385.82	386.14	−9.79	−9.79	3.15	3.53
Hole	$SCrSiN_2$	2.98	2.86	420.84	420.99	−5.94	−5.96	29.16	30.36
	$SeCrSiN_2$	3.21	3.03	403.19	403.54	−6.77	−6.77	18.74	19.83
	$TeCrSiN_2$	3.14	2.92	385.82	386.14	−8.66	−8.66	11.49	12.41

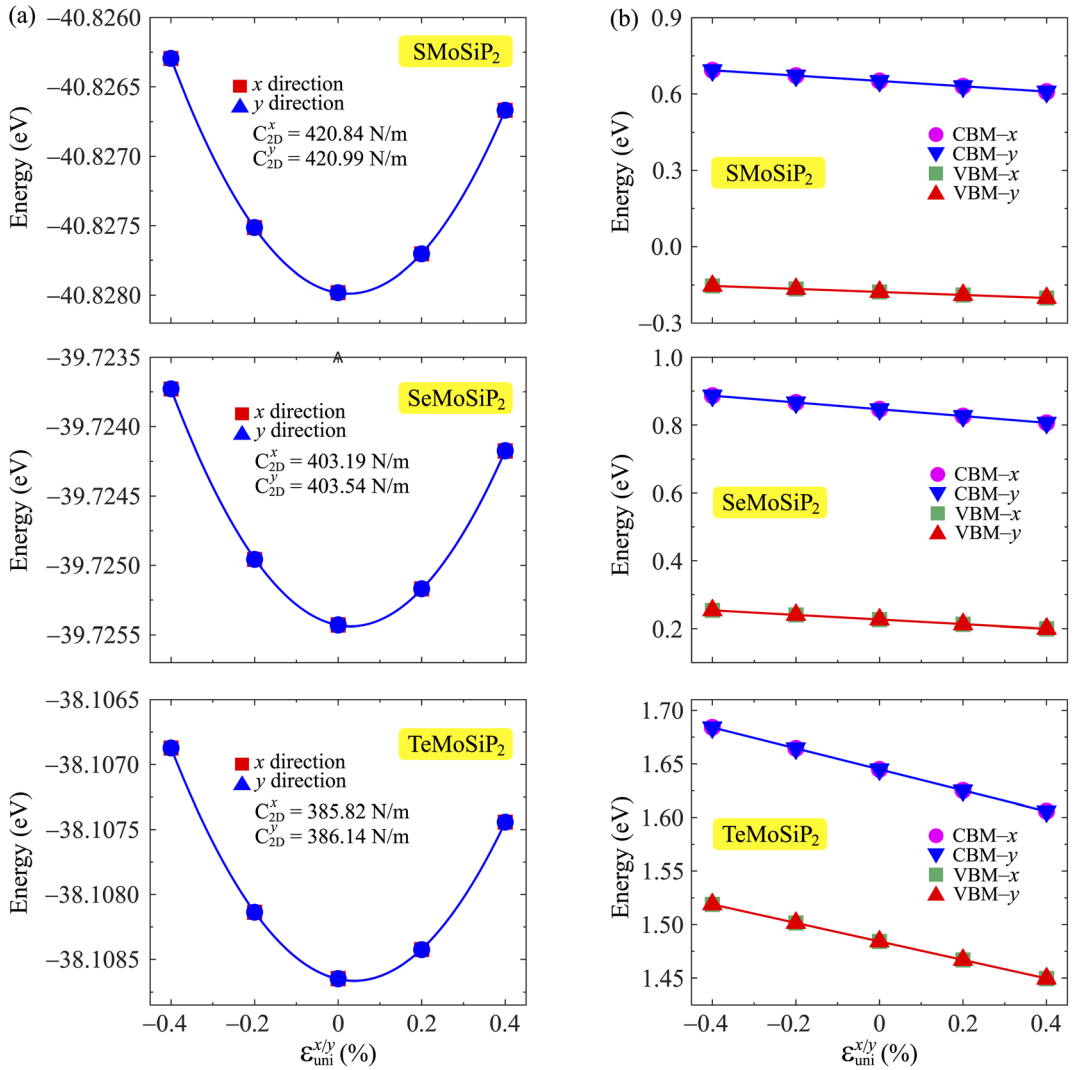

Fig. 10 The uniaxial strain-dependence $\varepsilon_{uni}^{x/y}$ of the total energies (a) and energies at the band edges (b) of $XCrSiN_2$ single-layers. Fitted data are shown by the solid line.

deformation potential approximation[30] and Boltzmann transport theory.[43] It should be emphasized that electron-phonon coupling (EPC) is significant in influencing the physical characteristics of materials, particularly thermoelectric properties and thermal conductivity.[44,45] In the present work, we only use the deformation potential (DP) approximation to evaluate the mobility of carriers. In the DP theory, the carrier mobility for 2D materials μ_{2D} is given by:[46]

$$\mu_{2D} = \frac{e\hbar^3 C_{2D}}{k_B T m^* \overline{m} E_d^2}, \quad (4)$$

where C_{2D} denotes the elastic modulus, E_d is the DP constant, k_B stands for the Boltzmann constant, e refers to the elementary charge, and $\hbar$ refers to the reduced Planck constant. m^* is the effective mass and $\overline{m} = \sqrt{m_x^* m_y^*}$ refers to the average effective mass. The DP constant E_d and elastic modulus C_{2D} are obtained by calculating the band edges and total energy, respectively, with respect to the uniaxial strain. The m^* of the carriers is calculated based on the dispersion of the CBM and VBM. The more dispersive area, the smaller the effective mass. In this study, the temperature T is set to be 300 K. All of the calculated values of effective mass, elastic modulus, DP constant, and mobility of carriers along the x and y directions are tabulated in Table 3.

The small uniaxial strain ε_{uni} (from −0.4 to +0.4%) is used to estimate the changing of total energy and the band edge positions. Fig. 10 illustrates the dependence of the total energies and the energies at the band edges on uniaxial strain ε_{uni}. From Fig. 10a, the total energies are found to alter insignificantly when the small uniaxial strain ε_{uni} is applied in the $x-$ or $y-$direction and has similar values in both directions. As for the elastic modulus, the highest value C_{2D} is found for $SMoSiN_2$, followed by that of $SeMoSiN_2$, then of $TeMoSiN_2$. It can be seen that for each structure, the elastic modulus C_{2D}^x and C_{2D}^y are nearly equal; in other words, the elastic modulus is essentially independent of the directions of uniaxial strains. However, it

can be observed from Fig. 10b that the band edge positions of $XMoSiN_2$ are almost the same along the directions of uniaxial strains. The deformation potential constants E_d listed in Table 3 indicate that for both electron and hole carriers, E_d is quite isotropic with the two in-plane transport directions. Consequently, the carrier mobilities are expected to be directional isotropy with the x and y transport directions.

Concerning directional isotropy, electron and hole mobilities for the x direction and y direction are similar. The electron mobilities in $SCrSiN_2$ and $SeCrSiN_2$ are much higher [67.01 (62.08) and 35.62 (34.44) $cm^2\ V^{-1}\ s^{-1}$ along the $x-$ ($y-$) direction] than that in $TeCrSiN_2$ [3.15 (3.53) $cm^2\ V^{-1}\ s^{-1}$ along the $x-$ ($y-$) direction]. As for hole mobilities, in both directions, higher values are found for the holes in the VBM of $SCrSiN_2$ and $SeCrSiN_2$, followed by that of $TeCrSiN_2$. These obtained mobilities demonstrate that the electrons and holes in $SCrSiN_2$ are all fast carriers with the highest migration abilities among the carriers in the three materials. Moreover, it is worth noting that in $SCrSiN_2$ and $SeCrSiN_2$ structures, the mobilities of electrons are greater than those of holes. However, in $SeCrSiN_2$ structures, it can be seen that the hole mobilities are higher compared to electron mobilities. This is mainly due to the differences of structural and chemical structures, specifically, the differences of dispersion profiles in the CBM and VBM in $XCrSiN_2$ single-layers as shown in Fig. 5 and 6; hence, the effective mass of electrons and holes is affected.

4 Conclusive remarks

In the current work, we explored the stabilities of the crystal structure, electronic properties, and transport features of the new quintuple $XCrSiN_2$ single-layers. The results show that the proposed Janus single-layers are energetically and thermally stable that reveal the potential to fabricate experimentally. All three structures exhibit semiconducting behavior with small indirect bandgaps. When biaxial strain is applied, the electronic structures of the Janus $XCrSiN_2$ single-layers are modulated significantly, especially, at $\varepsilon_b = -10\%$, and those of $SCrSiN_2$ single-layers are transmitted from the semiconductor to metal. Meanwhile, it is found that these proposed structures show weak dependence of their electronic bands on the electric field. The mobilities of electrons and holes are calculated indicating the highly directional isotropy due to the similarity in the effective masses. The mobility of electrons is higher than that of holes in $SCrSiN_2$ and $SeCrSiN_2$. The calculated results for mobility are found to be opposite for the $TeCrSiN_2$ case. Our proposed Janus quintuple $XCrSiN_2$ single-layers are promising 2D materials in the future with various applications.

Conflicts of interest

There are no conflicts of interest to declare.

Acknowledgements

This research was funded by the Vietnam Ministry of Education and Training under grant no. B2022-DNA-14.

References

1 Y. Guo, S. Zhou, Y. Bai and J. Zhao, *Appl. Phys. Lett.*, 2017, **110**, 163102.
2 A. Kandemir and H. Sahin, *Phys. Rev. B*, 2018, **97**, 155410.
3 Y. Bai, Q. Zhang, N. Xu, K. Deng and E. Kan, *Appl. Surf. Sci.*, 2019, **478**, 522–531.
4 W. Zhou, J. Chen, Z. Yang, J. Liu and F. Ouyang, *Phys. Rev. B*, 2019, **99**, 075160.
5 T. V. Vu, H. V. Phuc, A. I. Kartamyshev and N. N. Hieu, *Appl. Phys. Lett.*, 2023, **122**, 061601.
6 M.-Y. Liu, Y. He, X. Li and K. Xiong, *Phys. Chem. Chem. Phys.*, 2023, **25**, 7278–7288.
7 Y. Dahiya, M. Hariram, M. Kumar, A. Jain and D. Sarkar, *Coord. Chem. Rev.*, 2022, **451**, 214265.
8 L. Banszerus, M. Schmitz, S. Engels, J. Dauber, M. Oellers, F. Haupt, K. Watanabe, T. Taniguchi, B. Beschoten and C. Stampfer, *Sci. Adv.*, 2015, **1**, e1500222.
9 N. A. Poklonski, S. A. Vyrko, A. I. Siahlo, O. N. Poklonskaya, S. V. Ratkevich, N. N. Hieu and A. A. Kocherzhenko, *Mater. Res. Express*, 2019, **6**, 042002.
10 Q. H. Wang, K. Kalantar-Zadeh, A. Kis, J. N. Coleman and M. S. Strano, *Nat. Nanotechnol.*, 2012, **7**, 699.
11 C. V. Nguyen, N. N. Hieu, N. A. Poklonski, V. V. Ilyasov, L. Dinh, T. C. Phong, L. V. Tung and H. V. Phuc, *Phys. Rev. B*, 2017, **96**, 125411.
12 N. N. Hieu, H. V. Phuc, V. V. Ilyasov, N. D. Chien, N. A. Poklonski, N. V. Hieu and C. V. Nguyen, *J. Appl. Phys.*, 2017, **122**, 104301.
13 A. V. Lugovskoi, M. I. Katsnelson and A. N. Rudenko, *Phys. Rev. Lett.*, 2019, **123**, 176401.
14 V. T. Vi, N. N. Hieu, B. D. Hoi, N. T. Binh and T. V. Vu, *Superlattices Microstruct.*, 2020, **140**, 106435.
15 K. D. Pham, V. T. Vi, D. V. Thuan, N. V. Hieu, C. V. Nguyen, H. V. Phuc, B. D. Hoi, L. T. Phuong, N. Q. Cuong, D. V. Lu and N. N. Hieu, *Chem. Phys.*, 2019, **524**, 101–105.
16 F.-f. Zhu, W.-j. Chen, Y. Xu, C.-l. Gao, D.-d. Guan, C.-h. Liu, D. Qian, S.-C. Zhang and J.-f. Jia, *Nat. Mater.*, 2015, **14**, 1020–1025.
17 A. Acun, L. Zhang, P. Bampoulis, M. Farmanbar, A. van Houselt, A. N. Rudenko, M. Lingenfelder, G. Brocks, B. Poelsema, M. I. Katsnelson and H. J. W. Zandvliet, *J. Phys.: Condens. Matter*, 2015, **27**, 443002.
18 N. N. Hieu, H. V. Phuc, A. I. Kartamyshev and T. V. Vu, *Phys. Rev. B*, 2022, **105**, 075402.
19 T. V. Vu, V. T. T. Vi, H. V. Phuc, A. I. Kartamyshev and N. N. Hieu, *Phys. Rev. B*, 2021, **104**, 115410.
20 S.-D. Guo, W.-Q. Mu, Y.-T. Zhu, R.-Y. Han and W.-C. Ren, *J. Mater. Chem. C*, 2021, **9**, 2464–2473.
21 T. V. Vu and N. N. Hieu, *J. Condens.: Matter Phys.*, 2021, **34**, 115601.
22 H. Zhou, H. Tang, H. Yuan and H. Chen, *J. Magn. Magn. Mater.*, 2022, **562**, 169742.
23 Y. Gao, J. Liao, H. Wang, Y. Wu, Y. Li, K. Wang, C. Ma, S. Gong, T. Wang, X. Dong, Z. Jiao and Y. An, *Phys. Rev. Appl.*, 2022, **18**, 034033.

24 S.-T. Nguyen, C. Q. Nguyen, Y. S. Ang, H. V. Phuc, N. N. Hieu, N. T. Hiep, N. M. Hung, L. T. T. Phuong, N. V. Hieu and C. V. Nguyen, *J. Phys. D: Appl. Phys.*, 2022, **56**, 045306.
25 P. Giannozzi, S. Baroni, N. Bonini, M. Calandra, R. Car, C. Cavazzoni, D. Ceresoli, G. L. Chiarotti, M. Cococcioni, I. Dabo, A. D. Corso, S. de Gironcoli, S. Fabris, G. Fratesi, R. Gebauer, U. Gerstmann, C. Gougoussis, A. Kokalj, M. Lazzeri, L. Martin-Samos, N. Marzari, F. Mauri, R. Mazzarello, S. Paolini, A. Pasquarello, L. Paulatto, C. Sbraccia, S. Scandolo, G. Sclauzero, A. P. Seitsonen, A. Smogunov, P. Umari and R. M. Wentzcovitch, *J. Phys.: Condens. Matter*, 2009, **21**, 395502.
26 J. P. Perdew, K. Burke and M. Ernzerhof, *Phys. Rev. Lett.*, 1996, **77**, 3865.
27 H. J. Monkhorst and J. D. Pack, *Phys. Rev. B*, 1976, **13**, 5188–5192.
28 S. Grimme, J. Antony, S. Ehrlich and H. Krieg, *J. Chem. Phys.*, 2010, **132**, 154104.
29 S. Nosé, *J. Chem. Phys.*, 1984, **81**, 511.
30 J. Bardeen and W. Shockley, *Phys. Rev.*, 1950, **80**, 72.
31 L. Wang, Y. Shi, M. Liu, A. Zhang, Y.-L. Hong, R. Li, Q. Gao, M. Chen, W. Ren, H.-M. Cheng, Y. Li and X.-Q. Chen, *Nat. Commun.*, 2021, **12**, 2361.
32 M. Born and K. Huang, *Am. J. Phys.*, 1955, **23**, 474.
33 R. C. Andrew, R. E. Mapasha, A. M. Ukpong and N. Chetty, *Phys. Rev. B*, 2012, **85**, 125428.
34 N. T. Hung, A. R. T. Nugraha and R. Saito, *J. Phys. D: Appl. Phys.*, 2018, **51**, 075306.
35 P. Xiang, S. Sharma, Z. M. Wang, J. Wu and U. Schwingenschlögl, *ACS Appl. Mater. Interfaces*, 2020, **12**, 30731.
36 D. G. Pettifor, *Mater. Sci. Technol.*, 1992, **8**, 345–349.
37 L. Bengtsson, *Phys. Rev. B*, 1999, **59**, 12301.
38 H. Liu, Z. Huang, C. He, Y. Wu, L. Xue, C. Tang, X. Qi and J. Zhong, *J. Appl. Phys.*, 2018, **125**, 082516.
39 D. Q. Khoa, D. T. Nguyen, C. V. Nguyen, V. T. Vi, H. V. Phuc, L. T. Phuong, B. D. Hoi and N. N. Hieu, *Chem. Phys.*, 2019, **516**, 213–217.
40 T. V. Vu, V. T. T. Vi, C. V. Nguyen, H. V. Phuc and N. N. Hieu, *J. Phys. D: Appl. Phys.*, 2020, **53**, 455302.
41 T. V. Vu, V. T. T. Vi, H. V. Phuc, C. V. Nguyen, N. A. Poklonski, C. A. Duque, D. P. Rai, B. D. Hoi and N. N. Hieu, *J. Phys.: Condens. Matter*, 2021, **33**, 225503.
42 T. V. Vu, C. V. Nguyen, H. V. Phuc, A. A. Lavrentyev, O. Y. Khyzhun, N. V. Hieu, M. M. Obeid, D. P. Rai, H. D. Tong and N. N. Hieu, *Phys. Rev. B*, 2021, **103**, 085422.
43 B. Zeng, M. Li, X. Zhang, Y. Yi, L. Fu and M. Long, *J. Phys. Chem. C*, 2016, **120**, 25037–25042.
44 S. Qi, J. Liu, Y. Li and M. Zhao, *Phys. Rev. B*, 2022, **106**, 165204.
45 A. Giri, P. Karna and P. E. Hopkins, *J. Phys. Chem. Lett.*, 2022, **13**, 10918–10923.
46 W. Wan, S. Zhao, Y. Ge and Y. Liu, *J. Phys.: Condens. Matter*, 2019, **31**, 435501.